SCIENCE CHINA
Earth Sciences

•ARTICLE•

October 2025 Vol.68 No.10: 3216–3231
https://doi.org/10.1007/s11430-024-1659-9

Shallow shear wave velocity and radial anisotropy structure in the Binchuan basin, Yunnan Province, China, from ambient noise tomography

Kaifeng ZHAO[1,2], Jinchang FU[1], Hongfeng YANG[3], Xiaozhou YANG[1,2], Risheng CHU[4] & Yinhe LUO[1,2*]

[1] *Hubei Subsurface Multi-scale Imaging Key Laboratory, School of Geophysics and Geomatics, China University of Geosciences (Wuhan), Wuhan 430074, China*
[2] *State Key Laboratory of Geological Processes and Mineral Resources, China University of Geosciences, Wuhan 430074, China*
[3] *Department of Earth and Environmental Sciences, The Chinese University of Hong Kong, Hong Kong 999077, China*
[4] *State Key Laboratory of Precision Geodesy, Innovation Academy for Precision Measurement Science and Technology, Chinese Academy of Sciences, Wuhan 430077, China*

Received December 9, 2024; revised July 13, 2025; accepted August 5, 2025; published online September 18, 2025

Abstract Radial anisotropy structures are essential for understanding tectonic stress fields and distinguishing between low-velocity zones (LVZs) associated with sedimentary basins and fault damage zones, offering critical insights for comprehensive seismic hazard assessments. This study employed ambient noise tomography to investigate the fault zone and surrounding structures of the Chenghai Fault in the Binchuan Basin, Yunnan Province, China. Utilizing three-component waveform data collected from a linear dense seismic array consisting of 114 stations, we constructed a high-resolution shear wave velocity and radial anisotropy model. Our results reveal notable variations in radial anisotropy across the study region, with pronounced negative radial anisotropy surrounding the Chenghai Fault, likely reflecting fault damage. In contrast, positive radial anisotropy is observed beneath the Dongshan Mountain, indicative of extensional stress. The LVZ beneath the Binchuan Basin exhibits positive radial anisotropy, suggesting that this LVZ is primarily due to sedimentary deposits. Based on the shear wave velocity and radial anisotropy structure, we infer that the Chenghai Fault, influenced by east-west extensional tectonics, behaves as a high-angle normal fault. Additionally, another fault with a relatively lower dip angle is identified within the Binchuan Basin. The tectonic activity of the Chenghai Fault played a significant role in the initiation of sedimentation within the Binchuan Basin during the Neogene period. These findings are crucial for advancing the understanding of fault dynamics and provide essential insights for refining seismic hazard assessments in the region.

Keywords Binchuan Basin, Ambient noise tomography, Radial anisotropy, Seismic dense array, Fault damage zone

Citation: Zhao K, Fu J, Yang H, Yang X, Chu R, Luo Y. 2025. Shallow shear wave velocity and radial anisotropy structure in the Binchuan basin, Yunnan Province, China, from ambient noise tomography. Science China Earth Sciences, 68(10): 3216–3231, https://doi.org/10.1007/s11430-024-1659-9

1. Introduction

Earthquakes occur primarily along faults where accumulated stress is suddenly released, causing rupture. The kinematics of these earthquakes, including rupture direction, speed, and magnitude, are strongly influenced by the fault geometry, the tectonic stress field, and low-velocity zones (LVZs) adjacent to the fault (Barr and Houseman, 1992; Ben-Zion and Sammis, 2003; Huang and Ampuero, 2011; Yang et al., 2014). Understanding the distribution and direction of the

* Corresponding author (email: luoyinhe@cug.edu.cn)

tectonic stress field is crucial, as it determines the locations of stress concentration zones that govern the preferred propagation and termination points of ruptures (Yamashita, 2000; Dalguer et al., 2003). Additionally, the presence of fluids and fractures within the fault zone alters the frictional properties of the fault surface, further affecting rupture behavior (Eberhart-Phillips et al., 1995; Faulkner et al., 2010). LVZs can also amplify and prolong seismic waves, complicating rupture dynamics and influencing seismic site response (Weng et al., 2016; Chen and Yang, 2020; Song and Yang, 2022). Comprehending the interactions between stress fields, fault damage zone characteristics, and the effects of LVZs is essential for improving earthquake hazard assessments.

Ambient noise tomography is a primary method for studying fault zone properties (e.g., Gu et al., 2019; Gkogkas et al., 2021; Luo et al., 2022). However, relying solely on isotropic velocity structures presents challenges, particularly when trying to distinguish between LVZs associated with fault damage zone and those caused by shallow sediments, as both can exhibit similar low-velocity characteristics (e.g., Yang et al., 2020). Radial anisotropy, derived from the difference of shear wave velocities (V_{sh} and V_{sv}), offers crucial insights into the underlying stress fields (e.g., Nataf et al., 1986; Silver and Chan, 1988). Additionally, due to the differing orientations of layers and fractures, sediments and fault zones may exhibit distinct radial anisotropy properties (Luo et al., 2013; Shirzad et al., 2017; Naghavi et al., 2019; Wu et al., 2025). Therefore, constructing a high-resolution anisotropic velocity model of fault zones and surrounding region is essential for advancing our understanding of fault damage mechanisms and the distribution of LVZs.

The Chenghai Fault is a major tectonic unit in the rift zone of northwest Yunnan Province, China, characterized by frequent seismic activity. This fault extends in a north-south direction along the southeastern margin of the Tibetan Plateau and is associated with a series of east-west trending extensional basins that developed during the Quaternary period. Influenced by the tectonic evolution of the Tibetan Plateau, the Chenghai Fault Zone has experienced complex tectonic processes, including cycles of compression and extension since its formation in the Ordovician period (Chen et al., 2000; Hu et al., 2012). The fault exhibits left-lateral strike-slip motion and shows significant segmentation (Huang et al., 2018). Historically, the region has experienced numerous earthquakes with magnitudes exceeding 6.0 (Luo R J et al., 2015; Zhang and Liu, 2016; Huang et al., 2018). The Binchuan Basin, located west of the Chenghai Fault, has been shaped by the extension and shearing forces along the southern segment. Given this complex tectonic process of this regions, ongoing debates about the fault's evolutionary mechanisms underscore the need for further investigation (Liu et al., 1986; Li et al., 2013; Wang et al., 2023).

Numerous studies have constructed the crust and upper mantle velocity structure of the Chenghai Fault Zone and surrounding area (e.g., Zhang et al., 2005; Hu et al., 2005; Zhang and Wang, 2009; Wang et al., 2010; Wang and Gao, 2014; Liu et al., 2014; Bao et al., 2015; Zhang et al., 2020; Li et al., 2025). However, most of these studies primarily focus on the lower crustal and upper mantle structures using seismic stations with large interstation distances, resulting in relatively lower resolution of the study region. To enhance the understanding of the shallow structure in the Binchuan Basin, several studies have employed dense array to construct high-resolution shear wave velocity models. For instance, Yang et al. (2020) utilized ambient noise tomography with a linear dense array across the southern segment of the Chenghai Fault Zone in the Binchuan Basin, revealing a LVZ approximately 3.5 km wide surrounding the fault zone. Zhang Y P et al. (2023) conducted active source investigations and revealed along-strike variations of the LVZs along the Chenghai Fault. Sun et al. (2024) utilized receiver function analysis to construct the shallow structure of the Chenghai Fault Zone and proposed a multi-stage model for the evolution of the Binchuan Basin. Although these studies offer important insights into the regional velocity structure, they primarily focus on isotropic seismic velocities and lack detailed analysis of the fault's spatial extension and the prevailing stress regime.

Constructing a high-resolution anisotropic shear wave velocity structure of the Chenghai Fault and Binchuan Basin is crucial for understanding the structure and assessing seismic hazards in this region. In this study, we use ambient noise tomography to develop the shear wave velocity and radial anisotropy structure of the Chenghai Fault zone and surrounding areas, utilizing three-component waveform data from 114 linear array stations recorded over approximately one month. Our results reveal significant negative radial anisotropy around the Chenghai Fault Zone, while most of the region beneath the dense array exhibits positive anisotropy. These results suggest an extensional stress regime and a sedimentary environment, highlighting the importance of understanding the fault's characteristics and their implications for regional seismicity.

2. Surface wave from ambient noise

2.1 The cross-correlation functions

This study utilized a dense linear seismic array consisting of 114 seismic stations equipped with 5-second EPS instruments, deployed across the Chenghai Fault from January 6 to February 7, 2018, to investigate its structure. The interstation distance of this array is ~50 m, and the data were sampled at a rate of 20 Hz. Figure 1 shows the distribution of the stations alongside the relevant geological structures. We follow the

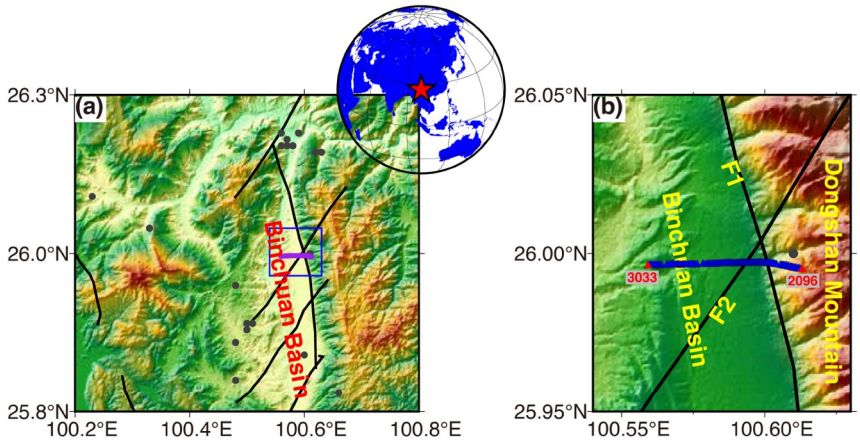

Figure 1 (a) Topography of the Binchuan Basin and the surrounding region. Black dots indicate earthquakes with magnitudes greater than 3.5, recorded from 1974 to 2023. Black lines represent faults within the region, blue box is the region plotted in (b), and the red star marks the location of the study area. Purple line is the dense array show in (b). (b) Map of the station distribution used in this study, with stations represented as triangles. F1 denotes the Chenghai Fault, while F2 denotes the Pianjiao-Binju Fault.

ambient noise data processing methods outlined by Bensen et al. (2007) and Lin et al. (2008) to obtain the ZZ and TT component cross-correlation functions (CCFs). After segmenting the waveforms into hourly intervals, we remove the mean and trend from the N, E, and Z component waveforms. We then normalize the hourly segments and employ a running-absolute-mean method in the time domain, followed by spectral whitening in the frequency domain to minimize the influence of earthquakes and other irregular peaks. We choose not to remove the instrument response for any waveforms since the same instrument was used consistently throughout this study. To preserve the relative amplitude relationships among the three components, we normalize each segment using the same value, which is determined by the maximum amplitude of the three components for that segment. We apply a band-pass filter to all segments at 0.125–2 s periods.

After completing the preprocessing, we calculate the CCFs for the ZZ, EN, EE, NN, and NE components using the N, E, and Z component waveforms. Subsequently, we rotate the NE, NN, EE, and EN hourly components into RR and TT components following the method outlined by Lin et al. (2008). Finally, we stack all hourly ZZ, TT and RR component CCFs using the time-frequency domain phase-weighted stacking method (Li et al., 2018) to form the final ZZ, TT and RR components CCFs. Figure 2 displays the CCFs for ZZ and TT components of station 3033 in relation to all other stations. The CCFs are presented for two-period bands of 0.25 s to 1 s, and 1 s to 2 s. The results indicate that the wavefields are complex at the period band of 0.25 to 1 s, with a notable change in the wavefront observed at approximately 2.9 km of interstation distance for both TT and ZZ components. Beyond this interstation distance, specific signal arrivals occur earlier than those observed between station pairs with shorter interstation distances. This phenomenon suggests the presence of internal noise sources within the linear array used at the period band of 0.25 to 1 s in this study. Additionally, by calculating the CCFs using continuous waveform data recorded during both daytime and nighttime, we observe that all results exhibit consistent patterns, which suggests that the influence of internal noise sources cannot be mitigated by selecting data from specific time intervals (Appendix Figures S1–S3). Previous studies suggest that this phenomenon can occur when a linear seismic array is placed across a road (e.g., Behm et al., 2013). In this study, we have identified two roads that intersect the dense seismic array vertically through satellite map analysis. One is a highway currently under construction, while the other is a national highway that plays a crucial role in local traffic. The locations and direction of these two roads within the dense array are illustrated in Figure 3. Based on the CCFs and the relative location of the road to the seismic stations, the national highway is identified as a prominent internal noise source within the array. Many studies have shown that dividing the dense array by road location is an effective way for mitigating this influence (e.g., Halliday et al., 2008; Nakata, 2016; Song et al., 2021). Figure 3 presents the CCFs from both on the west side (with the "virtual source" at station 3033) and the east side (with the "virtual source" at station 2096) of the national highway. We observe that the CCFs exhibit longer travel times as the interaction distance increases, which is typical behavior for CCFs. To facilitate further data analysis, we divide the dense array into two sections based on the location of the national highway. Additionally, because these two roads intersect our dense array approximately perpendicularly, placing the noise source within the Fresnel zone, the unilateral asymmetry of the noise source does not introduce any bias into the CCFs. As a

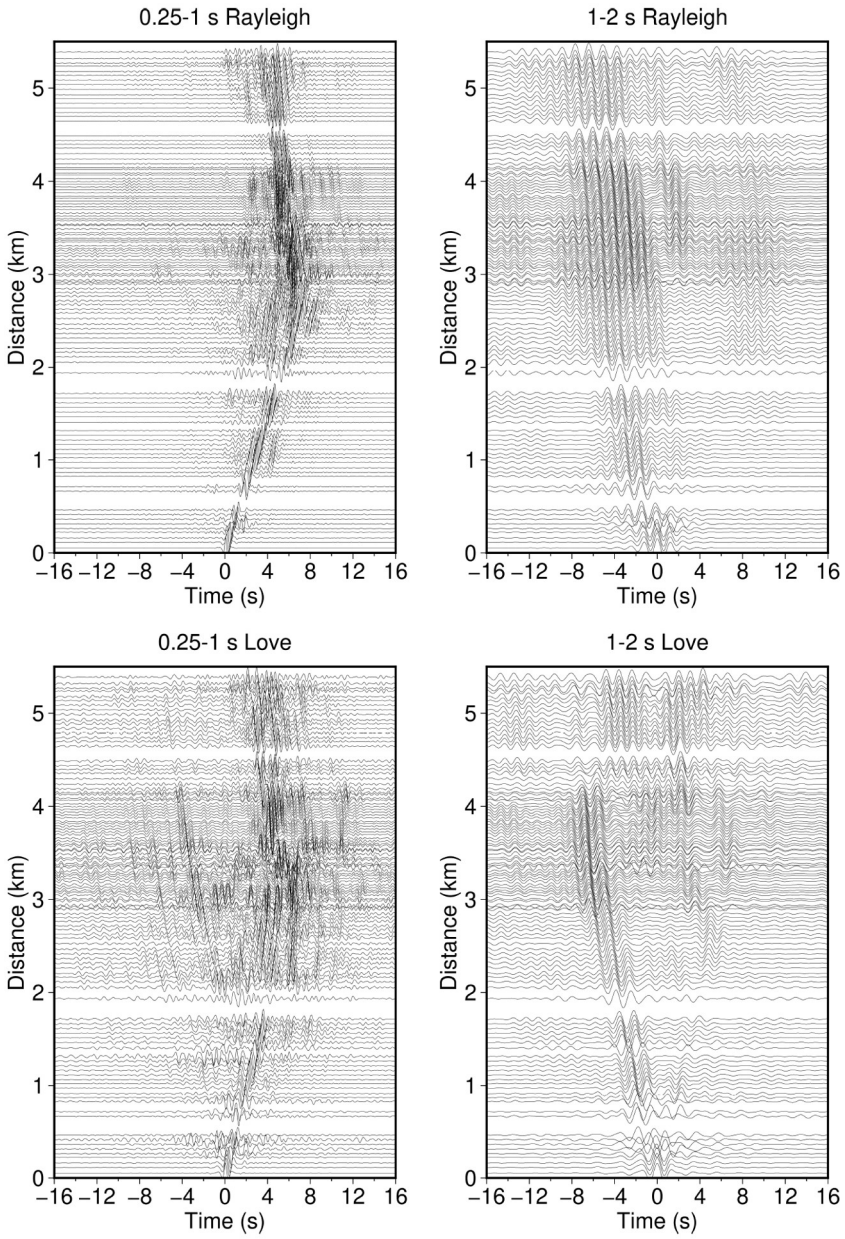

Figure 2 CCFs for the ZZ and TT components at station 3033, with respect to all other stations, at two different period bands: 0.25 to 1 s and 1 to 2 s.

result, this has a negligible impact on the measured dispersion curves, as well as on the final shear wave velocity and radial anisotropy models.

2.2 The phase velocity dispersion curves measured from CCFs

We employ the time-frequency analysis method (Bensen et al., 2007) to measure the Rayleigh and Love wave phase velocity dispersion curves from ZZ and TT component CCFs. A critical step in measuring these dispersion curves is resolving the circular ambiguity introduced by multiples of $2n\pi$, which necessitates a robust reference phase velocity model. To achieve this, we utilize the Frequency-Bessel method (Wang et al., 2019) to obtain average Rayleigh and Love phase velocity dispersion curves for each segment. This approach not only helps construct the reference model but also enhances us understanding of the distribution of multi-mode dispersion energy within the CCFs used in this study. For quality control, we only retain measurements with a signal-to-noise ratio (SNR) greater than 10, interstation distance longer than one wavelength (Luo Y H et al., 2015), and period range broader than 0.2 s considering the continuity of the dispersion curve. Here, the SNR is defined as the ratio of the maximum amplitude of signal window to the root mean square of the trailing noise window.

Figure 4 shows the measured phase velocity dispersion curves from both segments using ZZ and TT component CCFs. The background images in Figure 4 depict the dispersion energy constructed through the Frequency-Bessel method. The cutoff for the longest period is approximately 2 s (0.5 Hz) for most of the measured phase velocity dispersion curves, with notable variations in phase velocities for both Rayleigh and Love waves between the eastern and western segments of the national highway. If the velocity change of the measured dispersion curves is introduced by the noise source, it can be calculated by $v = v_{true} * \cos(\theta)$, where v_{true} is the true velocity, θ is the angle between the great-circle path of a station pair and the noise source. If the velocity change across the national highway were caused by a significant bias in the noise source distribution, the azimuth of the dominant noise sources would need to be misaligned with the dense array. The average phase velocity calculated by Frequency-Bessel transform method using all CCFs from each segment indicates that the phase velocities on the west side of the national highway are approximately 60% of those on the east side for Rayleigh and Love waves (Figure 4). Assuming the true velocities of both segments are identical, this suggests that the dominant noise sources are not located within the Fresnel zone and that their azimuths differ on either side of the road. However, according to our noise source analysis, the national highway is the dominant noise source and this road is nearly perpendicular to our array (Figure 3). Therefore, the angle between the great-circle path of the station pairs and the noise source is similar on both sides of the highway. This consistency in geometry indicates that the observed velocity differences are not caused by the noise source but are likely due to underlying geological variations. So this sharp contrast may be attributed to underlying geological structures, particularly evident in the eastern regions, where surface wave propagates across basins and mountainous areas, significantly influencing the characteristics of the observed phase velocity dispersion curves.

Another notable feature is the splitting of the Love wave phase velocity dispersion curves into two branches in the region of west of the national highway. To further investigate this phenomenon, we divide the dense array in this western part into two segments based on the under-construction highway. We observe that phase velocities change only when the ray paths cross the under-construction highway, suggesting that it may serve as an internal noise source affecting the Love wave phase velocity dispersion curves. This issue will be discussed further in Section 4.1. To enhance the accuracy of our phase velocity maps and reduce the influence of internal noise source, we divide the dense array into two segments for the Rayleigh wave analysis based on the relative location of the seismic station and the national highway. For the Love wave analysis, we divide the dense array into three segments based on the relative locations of the under-construction and national highways with respect to the seismic stations. In the subsequent tomography, we utilize only the dispersion curves from each segment.

2.3 The Rayleigh and Love wave phase velocity maps

We apply the ray-theory based surface wave tomography developed by Zhao et al. (2020) to construct phase velocity maps for Rayleigh and Love waves. Prior to perform tomography, we project all seismic stations onto a single straight line to accommodate any misalignments and facilitate analysis in 1-D grids. The tomography process divides the study area into uniform grids along this line. We calculate an average phase velocity by analyzing all dispersion curves at each period, which we then use to create an initial model. We apply the standard linearized inversion technique established by Tarantola and Valette (1982) to invert the phase velocities for each period along the 1-D grids. During inversion, the characteristic length of the 1-D Gaussian function is used to control the smoothness of the model, which is determined by the size of the grid and the results of the checkerboard tests.

As outlined in Section 2.2, we divide the dense array into two segments for Rayleigh waves and three segments for Love waves. This division leads to no ray paths crossing the gaps between these segments, making it necessary to perform tomography separately for each segment. In this study, we set the grid size to 150 m and employed a 1-D Gaussian function with a characteristic length of 200 m in the tomography. Firstly, we perform a series of tests to evaluate the resolution of our results and the appropriateness of the inversion parameters. Figure 5 and Figure 6 show the ray coverage and checkerboard test results for both Rayleigh and Love waves. The dense ray coverage allows the inversion to recover the model effectively, particularly in the eastern segments where the Chenghai Fault is located. Although a gap exists beneath the road in the western segment, its extent is smaller than the grid spacing used in the tomography. As a result, while the amplitude of the anomaly may not be fully recovered, the model remains reasonably well resolved, and the primary focus of this study is the Chenghai Fault Zone, which is located on the eastern side of the dense array. Additionally, although the ray density is relatively high in the central region of each segment, the longer wavelengths at longer periods result in fewer intersecting ray paths. This lack of cross-path coverage leads to suboptimal model recovery, particularly for Rayleigh waves, which have lower ray density. Figure 7 shows the phase velocity maps for Rayleigh waves ranging from 0.3 s to 1.2 s and for Love waves from 0.3 s to 1.6 s. To minimize the impact of the gap caused by splitting the array beneath the roads, we shade these areas in gray. The phase velocities for both waves are

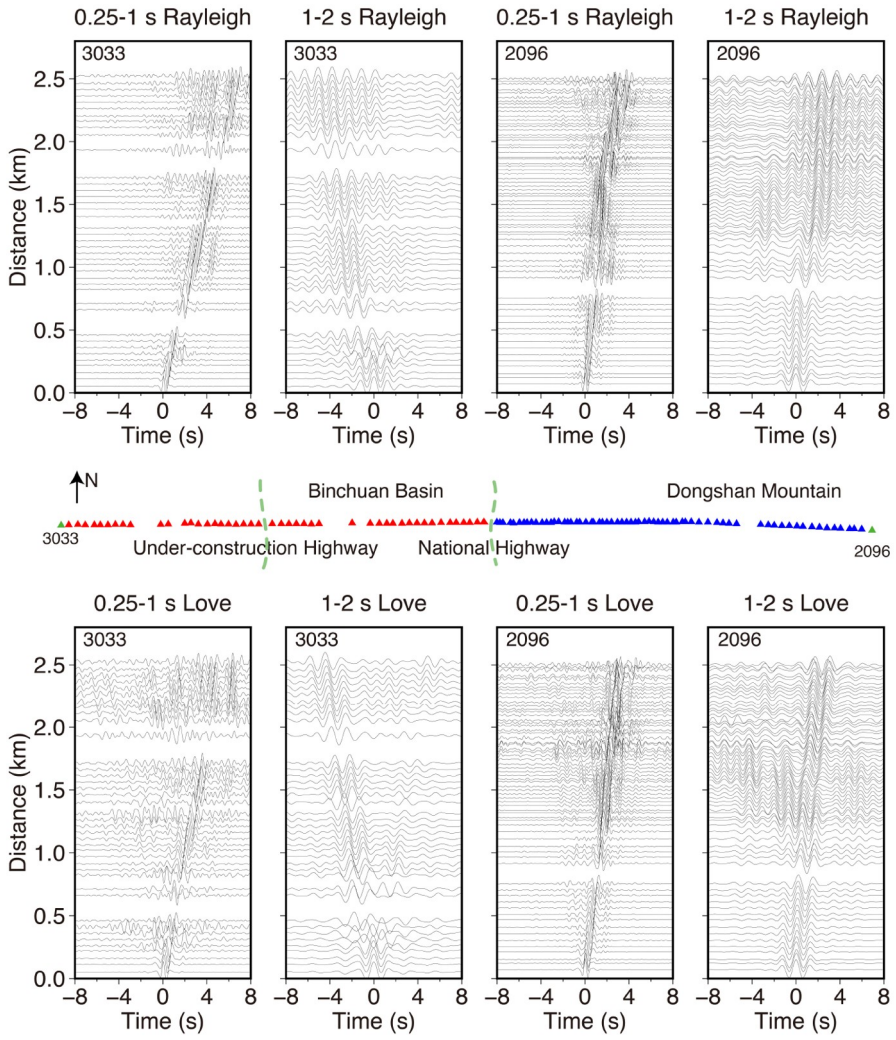

Figure 3 CCFs for the ZZ (Rayleigh waves) and TT (Love waves) components at station 3033, relative to all other stations (red triangles) located on the west side of the national highway, and at station 2096, relative to all other stations (blue triangles) located on the east side of the national highway, are shown for two distinct period bands: 0.25 to 1 s and 1 to 2 s. The green dashed lines represent the roads, and the green triangles represent the "virtual sources" at stations 3033 and 2096.

consistent with one another and align with the shallow geological structure. Lower phase velocities are observed in the western region where the Binchuan Basin is located, while higher velocities are found in the eastern region where the Dongshan Mountain is situated. Additionally, a noticeable phase velocity discontinuity occurs at the boundary between the basin and the mountain, corresponding to the Chenghai Fault belt on the eastern edge of the basin.

3. The shear wave velocity and radial anisotropy structure

After constructing phase velocity maps for Rayleigh and Love waves using ambient noise tomography, we employ the Least Squares Damping method (Herrmann and Ammon, 2004) to separately invert the V_{sv} and V_{sh} structures for each grid nodes. To determine the inversion depth, we calculate the sensitivity kernels of Rayleigh and Love waves to shear wave velocities. The results indicate that shorter-period surface wave phase velocities are sensitive to shallower shear wave velocities, while longer-period surface wave phase velocities are sensitive to deeper shear wave velocities (Figure 8). Specifically, Rayleigh waves with periods shorter than 1.2 s exhibit sensitivity to shallow structures at depths greater than 1 km, whereas Love waves are sensitive to even shallower structures. To leverage the advantages of both Rayleigh and Love waves, we set the inversion depth to 1 km.

An appropriate initial velocity model is crucial for the inversion process. However, constructing a suitable model for depths less than 1 km in the study area is challenging. To address this, we adopt the method proposed by Xu et al. (2012), which utilize an empirical relationship between

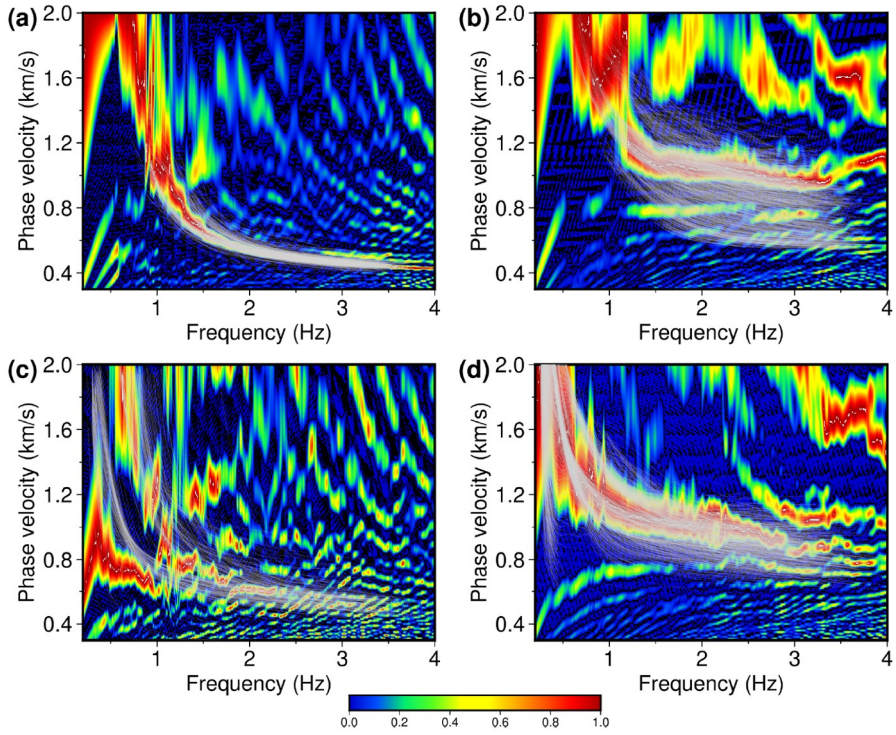

Figure 4 Dispersion curves and corresponding dispersion energy images for Rayleigh and Love waves. (a) and (b) display the Rayleigh wave dispersion curves extracted from the western and eastern segments, respectively. Similarly, (c) and (d) present the Love wave dispersion curves for the western and eastern segments, respectively. The background maps illustrate the dispersion energy images derived using the Frequency-Bessel transform method applied to all CCFs from each segment.

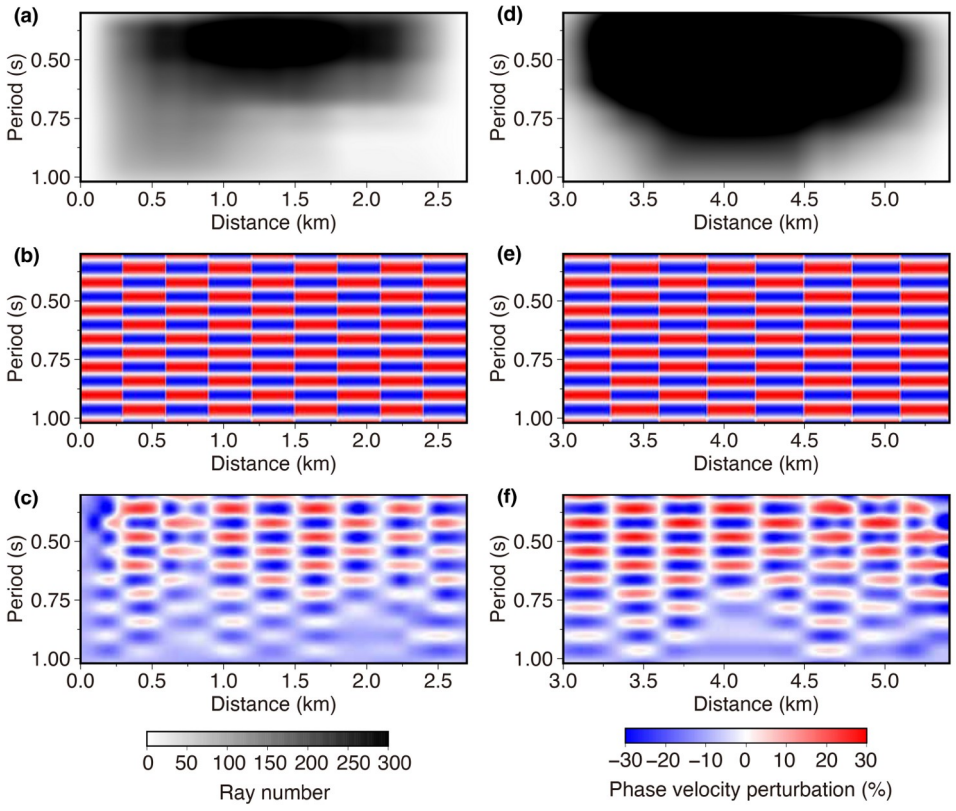

Figure 5 Ray density of Rayleigh waves in the western segment (a) and eastern segment (d), along with checkerboard tests for Rayleigh waves in the western segment (b, c) and eastern segment (e, f). (b) and (e) show the input models, while (c) and (f) present the corresponding inverted results.

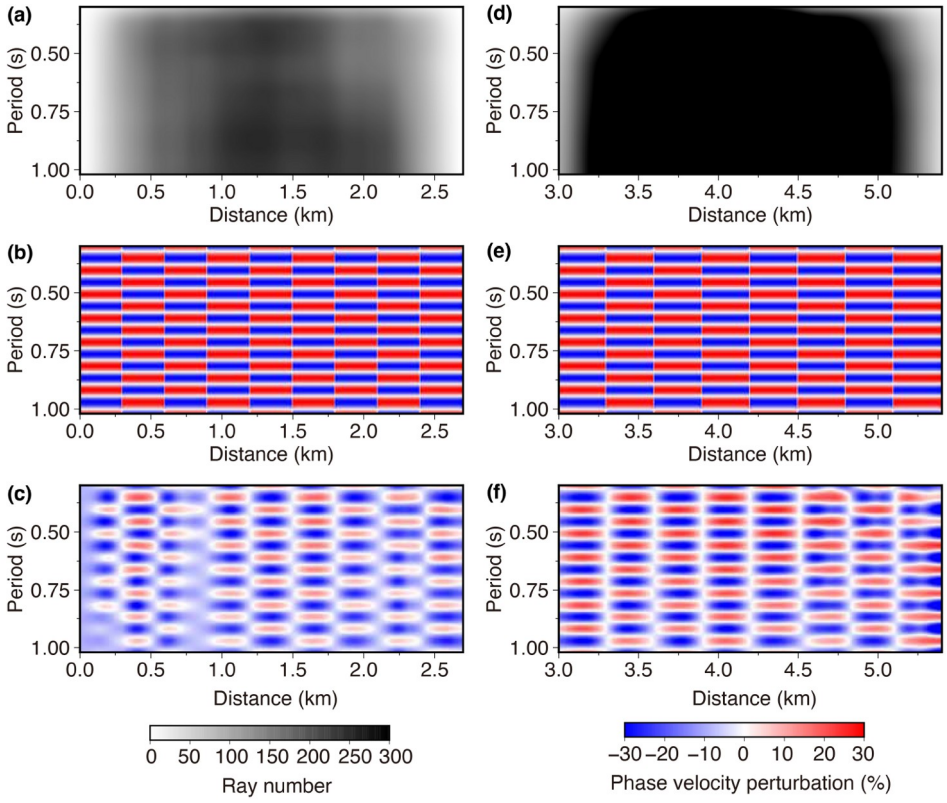

Figure 6 Similar with Figure 5 but for Love waves.

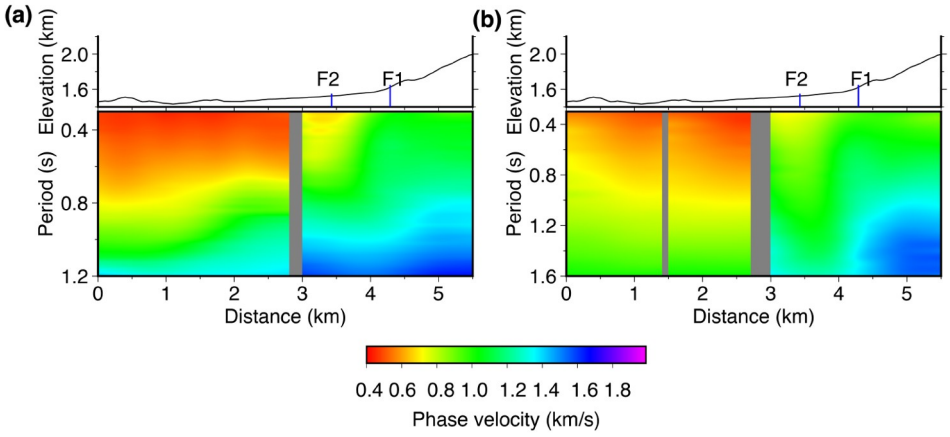

Figure 7 Phase velocity maps for Rayleigh waves (a) and Love waves (b) along the seismic array. F1 and F2 represent the faults.

phase velocity dispersion curves and shear wave velocities, to build the initial velocity model. We also establish a correspondence between shear wave velocities and their respective depths by assuming a relationship of h=0.6λ, where h is depth and λ is wavelength. The initial shear wave model consists of 10 layers, each with a thickness of 100 m. After constructing V_{sv} and V_{sh} structures by separately inverting the Rayleigh and Love wave phase velocity dispersion curves, we obtain the isotropic V_s structure by averaging the two, calculated as $V_s = \sqrt{\left(V_{sv}^2 + V_{sh}^2\right)/2}$. The radial anisotropy is calculated by $(V_{sh} - V_{sv})/V_s$. The resulting V_s and radial anisotropy model along the dense array is illustrated in Figure 9.

In Figure 9, the shear wave velocity across the study region reveals a general pattern of lower velocities on the western side and higher velocities on the eastern side. This distribution corresponds to the geographical features of the linear array area, with the western side aligned with the Binchuan Basin and the eastern side with the Dongshan Mountain. This pattern is consistent with results from other

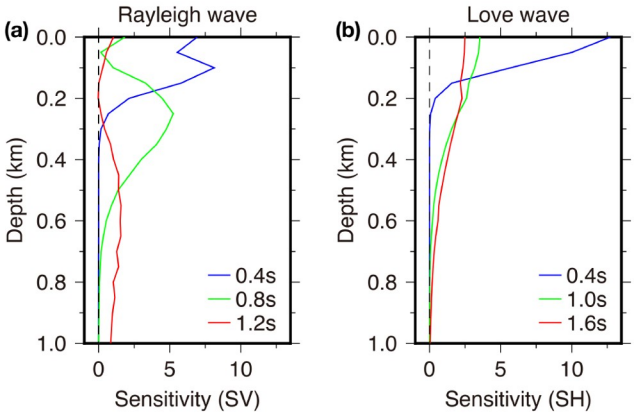

Figure 8 The sensitivity kernel of Rayleigh and Love wave phase velocities to shear wave velocities.

studies conducted at various locations within the Binchuan Basin based on surface and body waves (e.g., Zhang and Liu, 2016; Huang et al., 2018; Yang et al., 2020; Zhang Y P et al., 2023; Ma et al., 2024). Notably, significant variations are evident across the Chenghai fault zone, and an obvious "S"-shaped structure is observed. To assess the reliability of our inversion results, we have re-examined the velocity anomaly using two different initial models. These models were constructed based on the empirical relationships between phase velocity and shear wave velocity from Xia et al. (1999) and Xu et al. (2012). By inverting the shear wave velocities with these independent models, we consistently observe a clear "S"-shaped structure (Figure S4). This consistency between both models strongly supports the reliability of the observed structure. And through forward modeling and comparison of the dispersion curves derived from the shear wave velocity structure, both with and without the inclusion of the low-velocity anomaly in the shear wave velocity profile, we demonstrate that the observed structural features are not artifacts resulting from uncertainties in the dispersion measurements (Figure S5). Additionally, geological observations also indicate the presence of an "S"-shaped structure beneath the Chenghai Basin (Chun et al., 2006). Overall, the study region exhibits positive anisotropy, reflecting the extensional stress environment prevalent in the area. A prominent characteristic of radial anisotropy is observed near the Chenghai Fault Zone, where positive radial anisotropy is present at shallow depths, transitioning to negative anisotropy at greater depths.

4. Discussions

4.1 Distribution of the internal noise source in dense arrays

The calculation of CCFs from ambient noise data is on the assumption that noise sources are uniformly and randomly distributed. This assumption is crucial, as it allows the CCF to approximate the Empirical Green's Function (EGF) between two seismic stations (Snieder, 2004). However, when noise sources are unevenly distributed, such as when dominant noise originates from specific directions, this assumption is no longer valid. Consequently, CCFs may become biased, leading to systematic errors in measured phase velocity dispersion curves (e.g., Wang et al., 2016). These biases can significantly affect the accuracy of seismic velocity models derived from ambient noise tomography.

Based on the CCFs and the corresponding phase velocity dispersion curves measured from them, the national highway is identified as a prominent internal noise source contributing

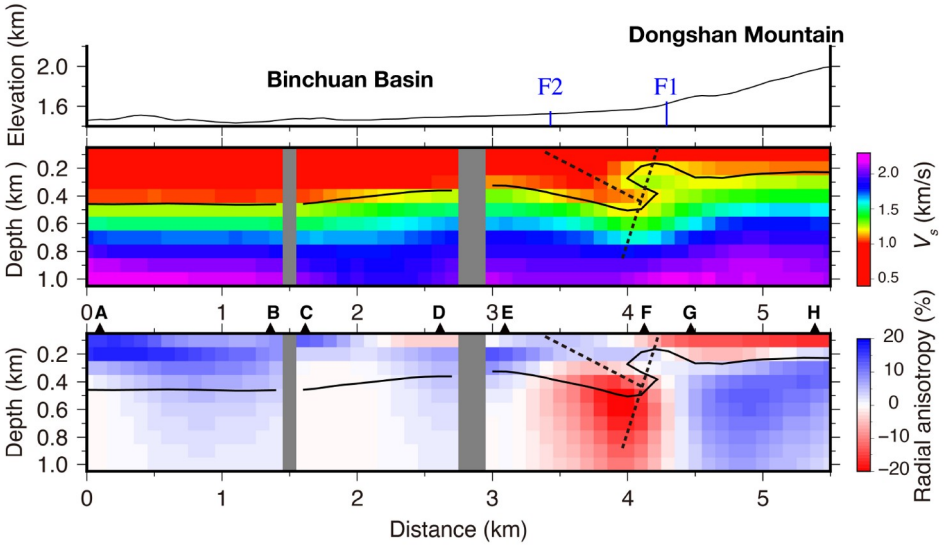

Figure 9 Shear wave velocity and radial anisotropy structure along the seismic array. The dashed lines represent the predicted faults, while the solid black lines delineate the boundary of the sedimentary basin, inferred from a velocity of 1.2 km/s. The black triangles represent selected stations along the array.

to the generation of Rayleigh waves, and the two highways that intersect the dense array may serve as noise sources for the Love waves. To further analyze the internal noise sources of Rayleigh and Love waves, we apply the beamforming method (e.g., Chen et al., 2002; Stehly et al., 2006) to analyze the azimuth distribution of noise source along the dense array. Compared to the higher azimuthal resolution achievable with 2-D dense arrays utilizing the beamforming method, the linear array employed in this study presents inherent limitations in accurately resolving the spatial energy distribution of noise sources across various directions. However, based on the linear array, we can still estimate the azimuth of noise sources and provide some indication of the direction from which the noise originates. Although other methods (e.g., Cheng et al., 2016; Pang et al., 2023; Zhang H et al., 2023; Guan et al., 2024; Hong et al., 2024) can effectively image the azimuth of noise sources using linear dense arrays, our analysis of the noise source characteristics and CCFs confirms that the national highway serves as the intermittent noise source and is nearly perpendicular to our array. Therefore, we did not employ these methods for further noise source imaging in this study.

According to the previous analysis in Section 2, we divide the dense array into three segments along the two roads to map the azimuthal distribution of Love waves, and into two segments along the national highway to image the azimuthal distribution of Rayleigh waves. Figure 10 shows the azimuthal distribution of Rayleigh and Love waves in different segments, based on beamforming method at 0.3 and 1 s. For Rayleigh waves (Figure 10a–10d), the results suggest that noise sources in both segments are directed toward the national highway, consistent with earlier discussion from the ZZ component CCFs.

According to the noise source azimuth distribution of Love waves in the array located in west of the under-construction highway and in the array between the under-construction highway and the national highway at 1 s (Figure 10h, 10i), clear noise sources are observed on both the east and west sides of these two subarrays. However, at 0.3 s, noise sources are primarily concentrated on the east side of these two subarrays. This suggests that both the under-construction highway and the national highway generate internal noise affecting the TT component CCFs, particularly near 1 s. Additionally, the noise source azimuth distribution of Love waves in the array located in east of the national highway at different frequencies shows a consistent westward direction (Figure 10g, 10j), indicating that the national highway acts as an internal noise source at different period bands.

Consequently, as described in sections 2.2 and 2.3 and based on the analysis of the noise source, we segment the array into three parts based on two roads crossing the dense array for Love wave analysis, and into two segments based on the relative location of the seismic station and the national highway for the Rayleigh wave analysis.

4.2 The reliability of radial anisotropy structure

From the radial anisotropy structure, we observe the amplitude of the radial anisotropy can reach up to 20%, significantly higher than those typically observed in the crust and upper mantle (Huang et al., 2010; Fu et al., 2015; Tan et al., 2015; Ling et al., 2017; Li et al., 2022). Therefore, before interpreting geological features based on these results, it is crucial to assess the accuracy of the radial anisotropy model. Due to the lack of a comparative radial anisotropy model for the shallow structure in our study area, we assess the accuracy of the radial anisotropy by analyzing the phase velocity dispersion curves of Rayleigh and Love waves measured from CCFs between selected station pairs (The triangle in Figure 9). We then invert these dispersion curves to calculate the radial anisotropy, following the same process outlined in Section 3.

Figure 11 presents the inverted V_{sv} and V_{sh} structures, the corresponding measured Rayleigh and Love wave dispersion curves, and the radial anisotropy derived from the difference between V_{sh} and V_{sv}. The selected station pairs used for this analysis are marked as triangles in Figure 9. We firstly compare the Radial anisotropy structures obtained from the inversion of dispersion curves measured from the CCFs of station pairs with those derived from the dispersion curves at the midpoint between two stations obtained by performing tomography. According to the results (The right column in Figure 11), the radial anisotropy derived from the measured phase velocity dispersion curves between station pairs aligns well with that derived from the dispersion curves after performing tomography. However, the amplitude of radial anisotropy inverted from these two types of dispersion curves shows notable differences in certain areas. This discrepancy arises because the measured dispersion curves reflect the average structure along the ray path.

In addition, we analyze the characteristics of the dispersion curves and the resulting inverted radial anisotropy structure. For example, when the phase velocity of Love waves exceeds that of Rayleigh waves at relatively shorter periods, notable positive radial anisotropy is observed. This effect is particularly pronounced when the ray path traverses regions of stronger radial anisotropy, such as the ray path between points A and B, where the difference in phase velocity between Rayleigh and Love waves becomes notably larger. According to the sensitivity kernels of Rayleigh and Love waves shown in Figure 8, Rayleigh waves are sensitive to deeper structures than Love waves at the same period. Therefore, if the phase velocity of Love waves is significantly greater than that of Rayleigh waves, it may indicate the presence of positive radial anisotropy. On the contrary, if the phase velocity difference between Rayleigh

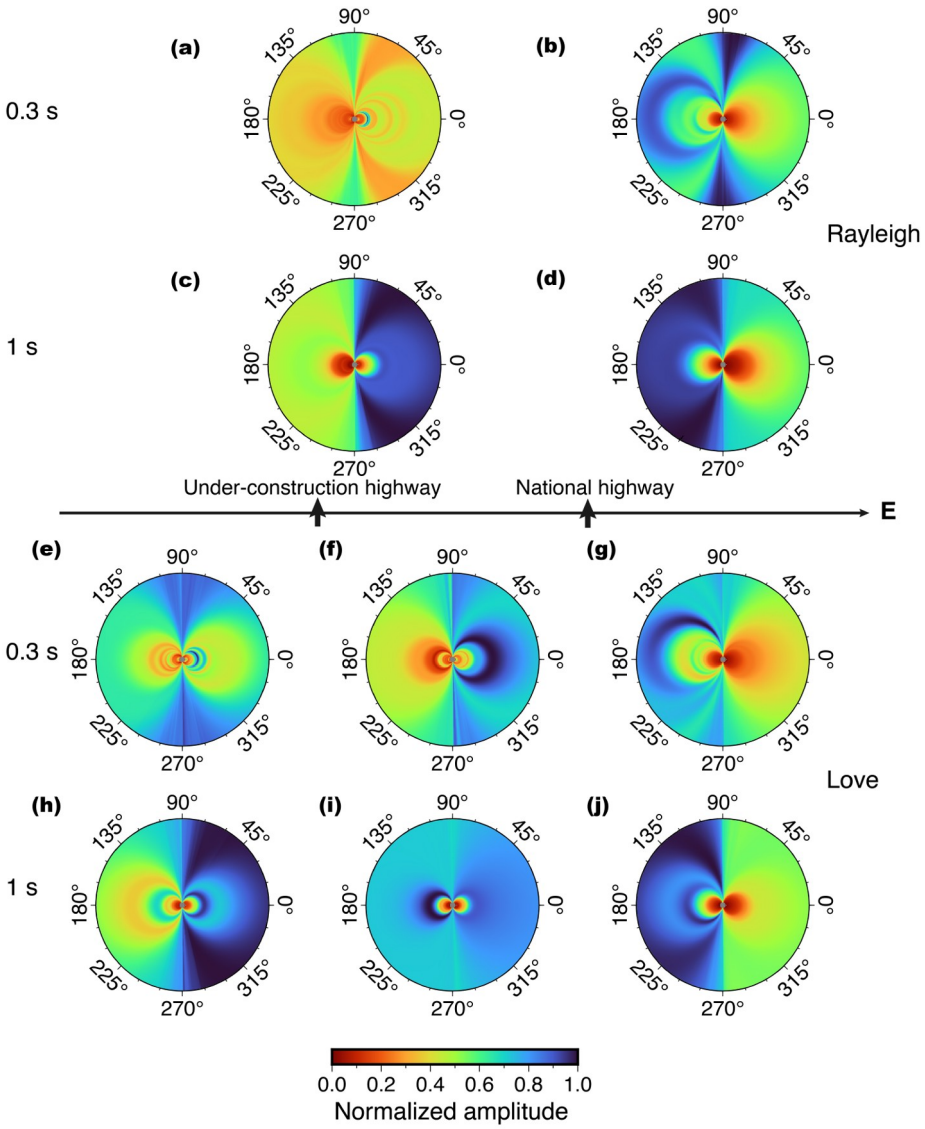

Figure 10 Noise distribution of Rayleigh and Love waves. Panels (a, c) show the noise sources for Rayleigh waves based on seismic stations located west of the national highway, while panels (b, d) show the results for stations located east of the national highway. Panels (e, h) represent the noise sources for Love waves based on seismic stations located west of the under-construction highway, and panels (f, i) show the results from stations situated between the under-construction highway and the national highway. Panels (g, j) display the results for seismic stations located east of the national highway.

and Love waves is small, as observed in the structures beneath station pairs CD and EF, we detect minimal radial anisotropy in the shallow subsurface. At longer periods, the phase velocity of Rayleigh waves is noticeably larger than that of Love waves across different station pairs. This may be attributed to the greater sensitivity depth of Rayleigh waves compared to Love waves, as well as the radial anisotropy of the structure beneath the station pair. To assess the characteristics of the measured dispersion curves for Rayleigh and Love waves, we also plot the dispersion curves derived from tomography at the midpoint of each station pair. The results indicate that the Rayleigh and Love wave dispersion curves are consistent with each other. This feature of the measured dispersion curves aligns with the observed radial anisotropy results, further validating the reliability of the anisotropic structure obtained through our inversion.

Previous studies on azimuthal anisotropy, such as Wang et al. (2024), indicate that around the Chenghai Fault, there is a pronounced azimuthal anisotropy, with the fast direction in our study region being consistent and approximately perpendicular to the dense array, parallel to the Chenghai Fault. The observed positive anisotropy at depths shallower than 300 m within the 3–4 km section of the survey line in this study is likely attributed to E-W extensional tectonics and may be consistent with the orientation of the azimuthal anisotropy observed by Wang et al. (2024). Additionally, the background positive radial anisotropy may have interfered with the strong negative radial anisotropy observed beneath

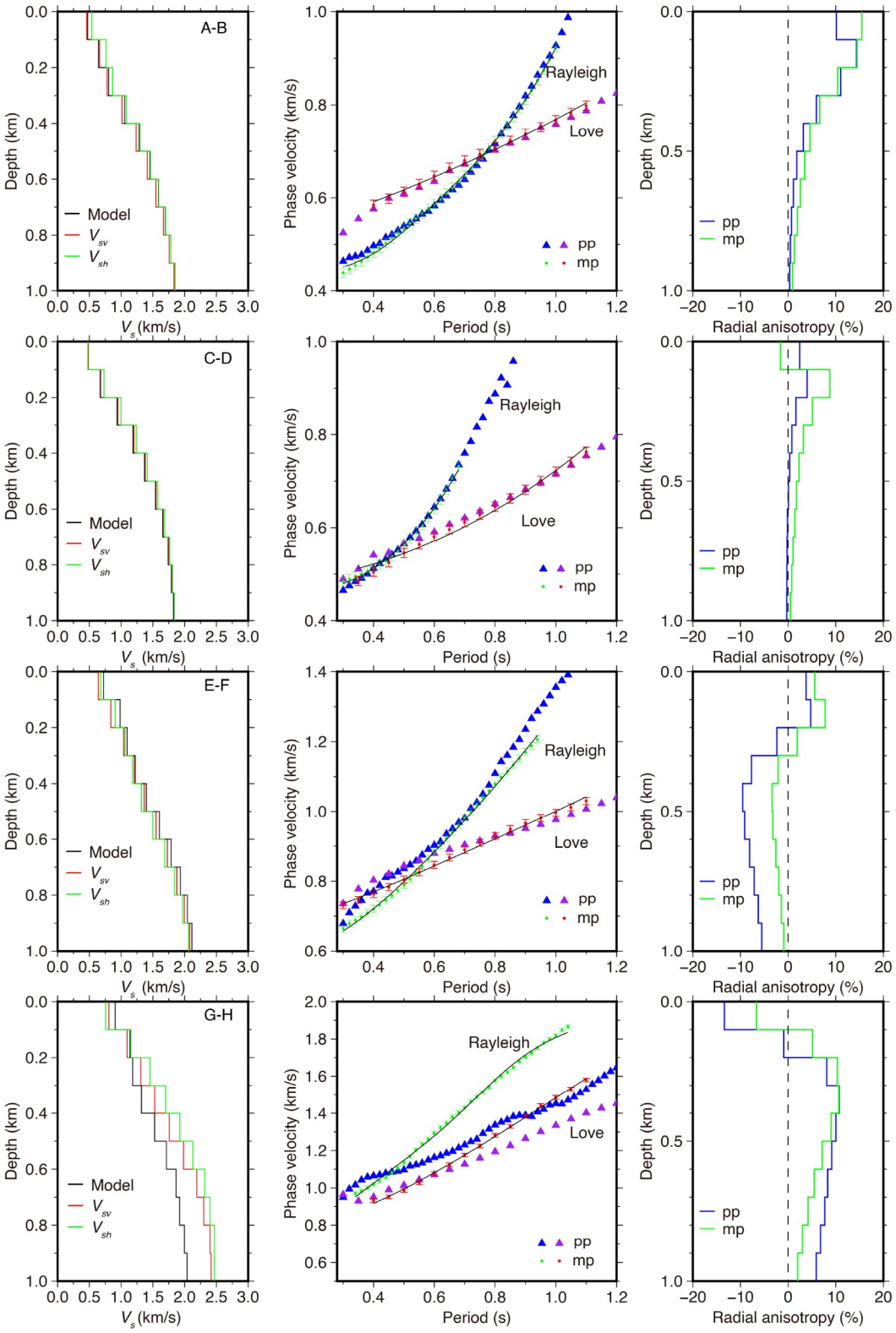

Figure 11 Shear wave velocity and radial anisotropy structure inverted from Rayleigh and Love wave dispersion curves for station pairs A-B, C-D, E-F, and G-H (shown as triangles in Figure 9). The left column presents the shear wave velocities inverted from the measured dispersion curves of station pairs, The middle column presents the Rayleigh and Love wave dispersion curves along different ray paths, as well as the dispersion curves at the midpoints of station pairs following tomography. Dots represent the measured dispersion curves between station pairs, black lines indicate the theoretical dispersion curves predicted by the inverted velocity structure shown in the left column, and triangles denote the dispersion curves extracted at the midpoints of station pairs after tomographic inversion. The right column is the inverted radial anisotropy. Results labeled "pp" are based on dispersion curves after tomography, with the point located at the midpoint of the ray path between stations. "mp" represents results inverted by the measured dispersion curves of the station pairs.

the Chenghai Fault (>300 m depth), potentially causing an underestimation of the true magnitude of the negative radial anisotropy. Further discussion on this positive radial anisotropy will be provided in Section 4.3.

4.3 The shallow structure of the Chenghai Fault and the surrounding region

The high-resolution structure of the Chenghai Fault Zone and Binchuan Basin plays a crucial role in advancing our understanding the geodynamic processes and in evaluating seismic hazards of the study region. Leveraging the dense array deployed across both the Chenghai Fault Zone and the Binchuan Basin, we have developed a high-resolution shear wave velocity and radial anisotropy model of the study region. Since surface waves are not highly sensitive to boundaries, it is challenging to precisely determine sediment thickness using surface wave tomography. Yang et al. (2020) applied ambient noise tomography with a dense array across the Chenghai Fault to construct the shallow structure of the Binchuan Basin. Their study identified a LVZ extending horizontally for 3.5 km and vertically for 1.6 km, using the 1.2 km/s contour line to estimate the sediment thickness. In this study, we refer to the results of Yang et al. (2020) and adopt this velocity threshold to determine the sediment thickness.

According to our results, the sediment thickness beneath our study region is approximately 500 m (the black lines in Figure 9), with maximum thickness below the Chenghai Fault. The average thickness of the Binchuan Basin is consistent with previous studies based on geological surveys (Huang et al., 2018), shear wave velocity structure (e.g., Zhang Y P et al., 2023) and receiver function (e.g., Sun et al., 2024), which suggest that the sediment thickness in our study area can reach up to 500 m, with the depositional center located on the eastern side of the basin.

Another notable feature of the shear wave structure is the relatively lower velocity beneath the Chenghai Fault compared to the surrounding region. Additionally, an "S-shaped" structure is observed around the fault, suggesting the presence of two faults with differing dip angles. Our results indicate that the Chenghai Fault has a steep dip angle, dipping westward, while an adjacent fault exhibits a relatively smaller dip angle, dipping eastward.

Radial anisotropy model along the dense array reveals large-scale positive radial anisotropy beneath the Binchuan Basin at relatively shallow depths and beneath the Dongshan Mountain at greater depths. In the Binchuan Basin, the positive radial anisotropy at relatively shallow depths aligns with the boundary of the LVZ, which is consistent with the typical radial anisotropy of sedimentary basins caused by horizontally layered sediments. This feature suggests that the LVZ in this region is primarily attributed to sedimentary materials rather than the fault damage zone. The positive radial anisotropy observed beneath Dongshan Mountain may be attributed to the regional background stress, consistent with the east-west extensional tectonics in the region (Tapponnier et al., 1986; Wang and Burchfiel, 1997; Cui et al., 2006). The pronounced east-west extensional features in northwestern Yunnan Province are likely driven by the westward rollback of the Burma Arc subduction zone and the lateral extrusion of lower crustal material from beneath the Tibetan Plateau (Wang et al., 2010; Liu et al., 2014). Additionally, we observe pronounced negative radial anisotropy beneath the Chenghai Fault and its surrounding areas. This may be attributed to the vertical displacement of fault blocks on either side of the fault, which likely promotes the development of fractures and fault-related damage zones. Geological observations suggest the Chenghai Fault is dominated by normal faulting and exhibits a left-lateral strike-slip component (e.g., Luo R J et al., 2015; Huang et al., 2018). Sun et al. (2024) also suggest that the evolution of the Binchuan Basin is controlled by the vertical displacement of the Chenghai Fault. These fractures, oriented along the fault plane and dip introduced by the vertical displacement of the Chenghai Fault, create zones of reduced seismic velocity, contributing to the observed negative radial anisotropy and relatively lower shear wave velocities in the fault damage zone.

In summary, utilizing shear wave velocity and radial anisotropy data, we construct the shallow structural model of the Chenghai Fault and its surrounding region (Figure 12). The Chenghai Fault, controlled by east-west extensional tectonics, functions as a high-angle normal fault. Additionally, another fault with a relatively small dip angle is present within the Binchuan Basin. Governed by the tectonic activity of the Chenghai Fault, the Binchuan Basin initiated sedimentation during the Neogene period. The extensional forces associated with the fault system caused gradual subsidence of the basin, generating significant accommodation space for sediment accumulation. Our result effectively distinguishes the LVZs associated with the sedimentary basin from those within the fault damage zone, while also providing detailed imaging of fault distribution. This differentiation is crucial for accurately assessing seismic hazards in the study area, as the seismic implications of LVZs in sedimentary basins (e.g., wave amplification) differ significantly from those in fault damage zones (e.g., fault activity and rupture potential).

5. Conclusion

In this study, we constructed the shallow shear wave and radial anisotropy structure of the Binchuan Basin and its surrounding area in Yunnan Province, China, using ambient

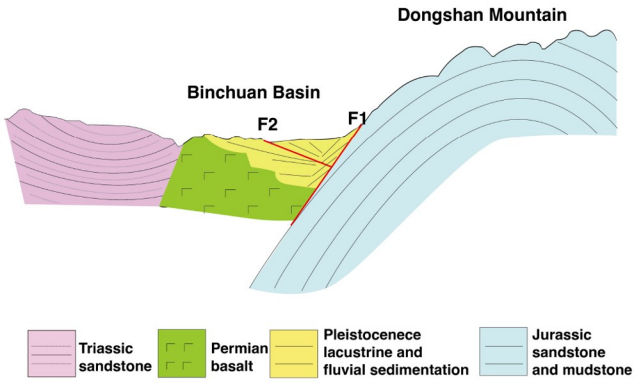

Figure 12 Schematic diagram illustrating the shallow structure of the study region (modified from Huang et al. (2021), we update the location of the F2 and the dip angle of F1 and F2).

noise tomography. Based on the inverted shear wave velocity and radial anisotropy models, we propose that the Chenghai Fault formed under east-west extensional stress. The LVZ beneath the Binchuan Basin exhibits positive radial anisotropy, suggesting that this LVZ is primarily due to sedimentary deposits within the basin. Additionally, we identified two faults near the Binchuan Basin with opposite dip angles: the Chenghai Fault, located on the eastern side of the Binchuan segment, is a high-angle fault dipping to the southwest, while its conjugate fault dips to the southeast at a relatively lower angle. These structural insights are crucial for assessing seismic hazards in the region, as they improve our understanding of fault dynamics and the distribution of LVZs, both critical for seismic risk evaluation.

Acknowledgements *This work was supported by the National Key Research and Development Program of China (Grant No. 2024YFF0807300), the National Natural Science Foundation of China (Grant Nos. 42474087, 42325401, 42488301), and the MOST Special Fund from the State Key Laboratory of Geological Processes and Mineral Resources, China University of Geosciences (Grant No. GPMR202447).*

Conflict of interest The authors declare no conflict of interest.

Supporting information The supporting information is available online at http://earth.scichina.com and http://link.springer.com. The supporting materials are published as submitted, without typesetting or editing. The responsibility for scientific accuracy and content remains entirely with the authors.

References

Bao X W, Sun X X, Xu M M, Eaton D W, Song X, Wang L, Ding Z, Mi N, Li H, Yu D, Huang Z, Wang P. 2015. Two crustal low-velocity channels beneath SE Tibet revealed by joint inversion of Rayleigh wave dispersion and receiver functions. Earth Planet Sci Lett, 415: 16–24

Barr T D, Houseman G A. 1992. Distribution of deformation around a fault in a non-linear ductile medium. Geophys Res Lett, 19: 1145–1148

Behm M, Leahy G M, Snieder R. 2013. Retrieval of local surface wave velocities from traffic noise: An example from the La Barge basin (Wyoming). Geophys Prospect, 62: 223–243

Bensen G D, Ritzwoller M H, Barmin M P, Levshin A L, Lin F C, Moschetti M P, Shapiro N M, Yang Y J. 2007. Processing seismic ambient noise data to obtain reliable broad-band surface wave dispersion measurements. Geophys J Int, 169: 1239–1260

Ben-Zion Y, Sammis C G. 2003. Characterization of fault zones. Pure Appl Geophys, 160: 677–715

Chen J C, Kung Yao J C, Hudson R E. 2002. Source localization and beamforming. IEEE Signal Process Mag, 19: 30–39

Cheng F, Xia J H, Luo Y H, Xu Z B, Wang L M, Shen C, Liu R F, Pan Y D, Mi B B, Hu Y. 2016. Multichannel analysis of passive surface waves based on crosscorrelations. Geophysics, 81: EN57–EN66

Chen X, Yang H. 2020. Effects of seismogenic width and low-velocity zones on estimating slip-weakening distance from near-fault ground deformation. Geophys J Int, 223: 1497–1510

Chen Z H, Burchfiel B C, Liu Y, King R W, Royden L H, Tang W, Wang E, Zhao J, Zhang X. 2000. Global Positioning System measurements from eastern Tibet and their implications for India/Eurasia intercontinental deformation. J Geophys Res, 105: 16215–16227

Chun F, Wang G, Wang S F, Wang E C. 2006. Structural interpretation of extensional deformation along the Dali fault system, southeastern margin of the Tibetan Plateau. Int Geol Rev, 48: 287–310

Cui X F, Xie F R, Zhang H Y. 2006. Recent tectonic stress field zoning in Sichuan-Yunnan region and its dynamic interest. Acta Seimol Sin, 19: 485–496

Dalguer L A, Irikura K, Riera J D. 2003. Simulation of tensile crack generation by three-dimensional dynamic shear rupture propagation during an earthquake. J Geophys Res, 108: 2001JB001738

Eberhart-Phillips D, Stanley W D, Rodriguez B D, Lutter W J. 1995. Surface seismic and electrical methods to detect fluids related to faulting. J Geophys Res, 100: 12919–12936

Faulkner D R, Jackson C A L, Lunn R J, Schlische R W, Shipton Z K, Wibberley C A J, Withjack M O. 2010. A review of recent developments concerning the structure, mechanics and fluid flow properties of fault zones. J Struct Geol, 32: 1557–1575

Fu Y V, Gao Y, Li A B, Shi Y T. 2015. Lithospheric shear wave velocity and radial anisotropy beneath the northern part of North China from surface wave dispersion analysis. Geochem Geophys Geosyst, 16: 2619–2636

Gkogkas K, Lin F C, Allam A A, Wang Y D. 2021. Shallow damage zone structure of the Wasatch Fault in Salt Lake City from ambient-noise double beamforming with a temporary linear array. Seismol Res Lett, 92: 2453–2463

Gu N, Wang K D, Gao J, Ding N, Yao H J, Zhang H J. 2019. Shallow crustal structure of the Tanlu fault zone near Chao Lake in Eastern China by direct surface wave tomography from local dense array ambient noise analysis. Pure Appl Geophys, 176: 1193–1206

Guan B, Xia J H, Pang J Y, Liu Y, Hong Y, Zhou J, Ma Y L. 2024. Improving data quality of three-component measurements of noise in urban environments using polarization analysis. IEEE Trans Geosci Remote Sens, 62: 5925610

Halliday D, Curtis A, Kragh E. 2008. Seismic surface waves in a suburban environment: Active and passive interferometric methods. Leading Edge, 27: 210–218

Herrmann, R. B, Ammon C J. 2004. Surface waves, receiver functions, and crustal structure. Computer Programs in Seismology, Version 3.30

Hong Y, Xia J H, Zhang H, Pang J Y, Guan B, Zhou J, Ma Y L. 2024. Azimuth correction for passive surface wave dispersion based on polarization analysis. Geophys J Int, 238: 1638–1650

Hu J F, Yang H Y, Xu X Q, Wen L M, Li G Q. 2012. Lithospheric structure and crust-mantle decoupling in the southeast edge of the Tibetan Plateau. Gondwana Res, 22: 1060–1067

Hu J F, Su Y J, Zhu X G, Chen Y. 2005. S-wave velocity and Poisson's ratio structure of crust in Yunnan and its implication. Sci China Ser D-Earth Sci, 48: 210–218

Huang H, Yao H J, van der Hilst R D. 2010. Radial anisotropy in the crust of SE Tibet and SW China from ambient noise interferometry. Geophys

Res Lett, 37: 2010GL044981
Huang X J, Wu Z H, Huang X L, Luo R J. 2018. Tectonic geomorphology constrains on Quaternary activity and segmentation along the Chenghai-Binchuan Fault Zone in Northwest Yunnan, China (in Chinese). Earth Sci, 43: 4651–4670
Huang X L, Wu Z H, Huang X J, Liu F, Wu K G. 2021. Late Cenozoic transtensional deformation along the Chenghai fault zone and its constraint on micro-block clockwise rotation in southeastern Tibetan Plateau. ESS Open Archive
Huang Y H, Ampuero J P. 2011. Pulse-like ruptures induced by low-velocity fault zones. J Geophys Res, 116: B12307
Li G L, Niu F L, Yang Y J, Xie J. 2018. An investigation of time-frequency domain phase-weighted stacking and its application to phase-velocity extraction from ambient noise's empirical Green's functions. Geophys J Int, 212: 1143–1156
Li M Y, Liu S L, Yang D H, Xu X W, Shen W H, Xie C D, Wang W S, Yang S X. 2022. Velocity structure and radial anisotropy beneath the northeastern Tibetan Plateau revealed by eikonal equation-based teleseismic P-wave traveltime tomography. Sci China Earth Sci, 65: 824–844
Li S H, Deng C D, Yao H T, Huang S, Liu C Y, He H Y, Pan Y X, Zhu R X. 2013. Magnetostratigraphy of the Dali Basin in Yunnan and implications for late Neogene rotation of the southeast margin of the Tibetan Plateau. J Geophys Res-Solid Earth, 118: 791–807
Li Z J, Wang Y, Liu L J, Shao Z G, Cheng F, Zhang J J, Gan W J, Hao M. 2025. Lithospheric deformation and corresponding deep geodynamic process of the SE Tibetan Plateau. Sci China Earth Sci, 68: 1303–1325
Lin F C, Moschetti M P, Ritzwoller M H. 2008. Surface wave tomography of the western United States from ambient seismic noise: Rayleigh and Love wave phase velocity maps. Geophys J Int, 173: 281–298
Ling Y, Chen L, Wei Z G, Jiang M M, Wang X. 2017. Crustal S-velocity structure and radial anisotropy beneath the southern part of central and western North China Craton and the adjacent Qilian Orogenic Belt from ambient noise tomography. Sci China Earth Sci, 60: 1752–1768
Liu G X, Li F Q, Li G R. 1986. Active tectonics and state of stress in seismic region of north-west Yunnan Province, China. Seismol Geol, 8: 1–14
Liu Q Y, van der Hilst R D, Li Y, Yao H J, Chen J H, Guo B, Qi S H, Wang J, Huang H, Li S C. 2014. Eastward expansion of the Tibetan Plateau by crustal flow and strain partitioning across faults. Nat Geosci, 7: 361–365
Luo R J, Wu Z H, Huang X L, Huang X J, Zhou C J, Tian T T. 2015. The main active faults and the active tectonic system of Binchuan area, northwestern Yunnan (in Chinese). Geol Bull China, 34: 155–170
Luo S, Yao H J, Zhang Z Q, Bem T S. 2022. High-resolution crustal and upper mantle shear-wave velocity structure beneath the central-southern Tanlu fault: Implications for its initiation and evolution. Earth Planet Sci Lett, 595: 117763
Luo Y H, Xu Y X, Yang Y J. 2013. Crustal radial anisotropy beneath the Dabie orogenic belt from ambient noise tomography. Geophys J Int, 195: 1149–1164
Luo Y H, Yang Y J, Xu Y X, Xu H R, Zhao K F, Wang K. 2015. On the limitations of interstation distances in ambient noise tomography. Geophys J Int, 201: 652–661
Ma X N, Yang W, Xu S H, Zhang Y P, Wang W T, Song J H, Liu C Y. 2024. Shallow characteristics of Chenghai Fault Zone, Yunnan, China, from ambient noise tomography and horizontal-to-vertical spectral ratio with two dense linear arrays. Tectonophysics, 881: 230351
Naghavi M, Hatami M R, Shirzad T, Rahimi H. 2019. Radial anisotropy in the upper crust beneath the Tehran Basin and surrounding regions. Pure Appl Geophys, 176: 787–800
Nakata N. 2016. Near-surface S-wave velocities estimated from traffic-induced Love waves using seismic interferometry with double beamforming. Interpretation, 4: SQ23–SQ31
Nataf H C, Nakanishi I, Anderson D L. 1986. Measurements of mantle wave velocities and inversion for lateral heterogeneities and anisotropy: 3. Inversion. J Geophys Res, 91: 7261–7307
Pang J Y, Xia J H, Cheng F, Zhou C J, Chen X H, Shen C, Xing H X, Chang X J. 2023. Surface wave dispersion measurement with polarization analysis using multicomponent seismic noise recorded by a 1-D linear array. Surv Geophys, 44: 1863–1895
Shirzad T, Shomali Z H, Riahi M A, Jarrahi M. 2017. Near surface radial anisotropy in the Rigan area/SE Iran. Tectonophysics, 694: 23–34
Silver P G, Chan W W. 1988. Implications for continental structure and evolution from seismic anisotropy. Nature, 335: 34–39
Snieder R. 2004. Extracting the Green's function from the correlation of coda waves: A derivation based on stationary phase. Phys Rev E, 69: 046610
Song J H, Yang H F. 2022. Seismic site response inferred from records at a dense linear array across the Chenghai fault zone, Binchuan, Yunnan. J Geophys Res-Solid Earth, 127: e2021JB022710
Song Z H, Zeng X F, Xie J, Bao F, Zhang G B. 2021. Sensing shallow structure and traffic noise with fiber-optic internet cables in an urban area. Surv Geophys, 42: 1401–1423
Stehly L, Campillo M, Shapiro N M. 2006. A study of the seismic noise from its long-range correlation properties. J Geophys Res, 111: B10306
Sun T W, Wang B S, Yang W. 2024. Fine shallow structures of Binchuan basin inverted from receiver functions and implications for Basin evolution. J Geophys Res-Solid Earth, 129: e2024JB028858
Tan J, Li H Y, Li X F, Zhou M, Ouyang L B, Sun S J, Zheng D. 2015. Radial anisotropy in the crust beneath the northeastern Tibetan Plateau from ambient noise tomography. J Earth Sci, 26: 864–871
Tapponnier P, Peltzer G, Armijo R. 1986. On the mechanics of the collision between India and Asia. Geol Soc London Spec Publ, 19: 113–157
Tarantola A, Valette B. 1982. Generalized nonlinear inverse problems solved using the least squares criterion. Rev Geophys, 20: 219–232
Wang C Y, Lou H, Silver P G, Zhu L P, Chang L J. 2010. Crustal structure variation along 30°N in the eastern Tibetan Plateau and its tectonic implications. Earth Planet Sci Lett, 289: 367–376
Wang E, Burchfiel B C. 1997. Interpretation of Cenozoic tectonics in the right-lateral accommodation zone between the Ailao Shan shear zone and the eastern Himalayan syntaxis. Int Geol Rev, 39: 191–219
Wang H, Yang Z Y, Liu Z J, Tong Y B, Jing X Q. 2023. Tectonic rotation pattern at the northern end of the Red River Fault system in SE Tibet: New Paleomagnetic evidence from Cretaceous red beds. Tectonics, 42: e2021TC007116
Wang J N, Wu G X, Chen X F. 2019. Frequency-Bessel transform method for effective imaging of higher-mode Rayleigh dispersion curves from ambient seismic noise data. J Geophys Res-Solid Earth, 124: 3708–3723
Wang J, Yao H J, Liu Y, Wang B, Wang W T. 2024. 3D shear wave velocity and azimuthal anisotropy structure in the shallow crust of Binchuan Basin in Yunnan, Southwest China, from ambient noise tomography. Earthquake Res Adv, 4: 100327
Wang K, Luo Y H, Yang Y J. 2016. Correction of phase velocity bias caused by strong directional noise sources in high-frequency ambient noise tomography: A case study in Karamay, China. Geophys J Int, 205: 715–727
Wang Q, Gao Y. 2014. Rayleigh wave phase velocity tomography and strong earthquake activity on the southeastern front of the Tibetan Plateau. Sci China Earth Sci, 57: 2532–2542
Weng H H, Yang H F, Zhang Z G, Chen X F. 2016. Earthquake rupture extents and coseismic slips promoted by damaged fault zones. J Geophys Res-Solid Earth, 121: 4446–4457
Wu P P, Guo H L, Xu W, Qin T W, Li D H, Lu L Y, Ding Z F. 2025. High-resolution velocity and seismic anisotropy structures of the 2021 M_s6.0 Luxian Earthquake Zone in Sichuan Basin. Seismol Res Lett, 96: 78–96
Xia J H, Miller R D, Park C B. 1999. Estimation of near-surface shear-wave velocity by inversion of Rayleigh waves. Geophysics, 64: 691–700
Xu P F, Ling S Q, Li C J, Du J G, Zhang D M, Xu X Q, Dai K M, Zhang Z H. 2012. Mapping deeply-buried geothermal faults using microtremor array analysis. Geophys J Int, 188: 115–122
Yamashita T. 2000. Generation of microcracks by dynamic shear rupture

and its effects on rupture growth and elastic wave radiation. Geophys J Int, 143: 395–406
Yang H F, Duan Y H, Song J H, Jiang X H, Tian X F, Yang W, Wang W T, Yang J. 2020. Fine structure of the Chenghai fault zone, Yunnan, China, constrained from teleseismic travel time and ambient noise tomography. J Geophys Res-Solid Earth, 125: e2020JB019565
Yang H F, Li Z F, Peng Z G, Ben-Zion Y, Vernon F. 2014. Low-velocity zones along the San Jacinto Fault, Southern California, from body waves recorded in dense linear arrays. J Geophys Res-Solid Earth, 119: 8976–8990
Zhang H, Mi B B, Liu Y, Xi C Q, Ning L. 2023. Weighted stacking of ambient noise correlations based on the coherency of 3C data. J Appl Geophys, 213: 105035
Zhang X, Wang Y H. 2009. Crustal and upper mantle velocity structure in Yunnan, Southwest China. Tectonophysics, 471: 171–185
Zhang Y, Liu J. 2016. Study on characteristics of fault activity and relation between fault activity and earthquakes in Yunnan region (in Chinese). J Geodesy Geodyn, 36: 485–489
Zhang Y P, Yang H F, Yang W, Wang W T, Ma X N. 2023. Along-strike variation in the shallow velocity structure beneath the Chenghai fault zone, Yunnan, China, constrained from methane sources and dense arrays. Seismol Res Lett, 94: 2273–2290
Zhang Z J, Bai Z M, Wang C Y, Teng J W, Lü Q T, Li J L, Sun S X, Wang X Z. 2005. Crustal structure of Gondwana- and Yangtze-typed blocks: An example by wide-angle seismic profile from Menglian to Malong in western Yunnan. Sci China Ser D-Earth Sci, 48: 1828–1836
Zhang Z Q, Yao H J, Yang Y. 2020. Shear wave velocity structure of the crust and upper mantle in Southeastern Tibet and its geodynamic implications. Sci China Earth Sci, 63: 1278–1293
Zhao K F, Yang Y J, Luo Y H. 2020. Broadband finite frequency ambient noise tomography: A case study in the western United States using USArray stations. J Geophys Res-Solid Earth, 125: e2019JB019314

(Editorial handling: Ling CHEN)